Origin of the Warm Arctic-Cold North American Pattern on the Intraseasonal Time Scale

Hai Lin, Bin Yu, Nicholas M. J. Hall

Origin of the Warm Arctic–Cold North American Pattern on the Intraseasonal Time Scale

HAI LIN,[a] BIN YU,[b] AND NICHOLAS M. J. HALL[c]

[a] *Recherche en prévision numérique atmosphérique, Environment and Climate Change Canada, Montreal, Quebec, Canada*
[b] *Climate Research Division, Environment and Climate Change Canada, Toronto, Ontario, Canada*
[c] *LEGOS, University of Toulouse/IRD/CNRS/CNES, Toulouse, France*

(Manuscript received 14 January 2022, in final form 25 April 2022)

ABSTRACT: The warm Arctic–cold continent pattern (WACC) of near-surface air temperature variability has often been associated with the connection between Arctic sea ice reduction and cold weather over the midlatitude continents. Whether the existence of this pattern is due to variability of sea ice or is caused by atmospheric internal dynamics is subject to debate. Based on a long integration of a primitive equation atmospheric model (SGCM), this study examines the origin of the warm Arctic–cold North American pattern (WACNA), which is characterized by a pair of opposite surface air temperature anomalies over the high-latitude Chukchi–Bering Sea region and the North American continent, in boreal winter on the intraseasonal time scale. The model atmosphere is maintained by a time-independent forcing, so that atmospheric internal dynamics is the only source of variability. It is found that the SGCM model simulates well the behavior of the observed WACNA pattern. The WACNA pattern develops by interacting with the time-mean flow and synoptic-scale transient eddies. Two pathways of Rossby wave propagation are associated with WACNA. The northern pathway originates from eastern Siberia moving eastward across the Bering Strait to Canada, and the southern pathway is rooted in the subtropical waveguide propagating across the eastern North Pacific. Our simulation of this pattern implies that tropospheric dynamics alone can generate the WACNA, and the predictability associated with this pattern is likely limited by its internal dynamics nature.

SIGNIFICANCE STATEMENT: The warm Arctic–cold continent pattern of temperature variability has often been associated with the connection between Arctic sea ice reduction and cold weather over the midlatitude continents, which implies possible impacts of polar warming on midlatitude climate. There has been debate on whether the existence of this pattern depends on variability of sea ice or can be caused by processes within the atmosphere. In this study, we use a simple atmospheric model, which has a constant forcing; thus, atmospheric internal dynamics is the only source of variability. We show that atmospheric internal dynamics alone can generate the warm Arctic–cold North American pattern. The result has implications for our understanding of the impact of global warming.

KEYWORDS: Atmospheric circulation; Climate variability; Internal variability; Intraseasonal variability; Rossby waves; Teleconnections

1. Introduction

The "warm Arctic–cold continent" pattern (WACC) is characterized by the concurrence of an anomalously warm Arctic and anomalously cold temperatures over midlatitude continents during boreal winter (e.g., Overland et al. 2011; Cohen et al. 2014; Mori et al. 2014; Kug et al. 2015; Sun et al. 2016). In the Northern Hemisphere, two pairs of WACC patterns are observed, i.e., the warm Arctic–cold Eurasia (WACE; e.g., Mori et al. 2014, 2019; Cohen et al. 2012; Sorokina et al. 2016) and warm Arctic–cold North America (WACNA; e.g., Blackport et al. 2019; Lin 2015, 2018; Guan et al. 2020a; Yu and Lin 2022). The WACC variability was found to exist on long-term trend (e.g., Sun et al. 2016; Sigmond and Fyfe 2016), interannual (e.g., Cohen et al. 2012; Yu and Lin 2022) and intraseasonal time scales (e.g., Kug et al. 2015; Lin 2015, 2018; Guan et al. 2020b).

As the Arctic warming is associated with sea ice loss and global warming, a number of studies suggested that the WACC pattern is driven by the sea ice loss which implies impacts of polar warming on midlatitude climate (e.g., Deser et al. 2007; Honda et al. 2009; Overland and Wang 2010; Francis and Vavrus 2012; Mori et al. 2014, 2019). In contrast, another group of studies argued that the Arctic sea ice variability has little contribution to midlatitude climate; instead, WACC results from atmospheric internal dynamics, and the Arctic sea ice change is a response to the atmospheric anomaly (e.g., Screen et al. 2013; Sorokina et al. 2016; Sun et al. 2016; Screen and Blackport 2019; Blackport et al. 2019). In addition, Yu and Lin (2022) reported that the interannual variability of WACNA is influenced by ENSO and anomalies of snow cover over Siberia. The WACC pattern was found to arise from the planetary-scale Rossby wave response to an enhanced gradient in convection over the tropical Pacific Ocean and its associated temperature advection (e.g., Clark and Lee 2019; Park and Lee 2021). On the intraseasonal

Denotes content that is immediately available upon publication as open access.

Corresponding author: Hai Lin, hai.lin@ec.gc.ca

DOI: 10.1175/JAS-D-22-0013.1

time scale, the WACNA was found to be associated with the Madden–Julian oscillation (MJO; e.g., Lin 2015; Guan et al. 2020b) and coupling between the troposphere and stratosphere (e.g., Guan et al. 2020b). However, what dynamical processes are essential to WACNA is still unclear. Although some previous studies suggested that the atmospheric internal dynamics is important, it remains to be explored if the internal dynamics alone can generate WACNA and what roles the mean flow and transient eddies play.

In this study, we examine the origin of WACNA using a simple primitive equation global atmospheric model (SGCM). The model atmosphere is maintained by a time-independent forcing, so that the atmospheric internal dynamics is the only source of variability. The model does not have representation of variability in sea ice, snow cover, sea surface temperature (SST), tropical convection associated with the MJO and of the stratosphere, which allows us to exclude these processes in generating WACNA in the model. We compare the dominant mode of intraseasonal temperature variability simulated by SGCM over the North American region with the observed WACNA pattern. The roles of time-mean flow and synoptic-scale transient eddies on the WACNA pattern are also investigated.

Section 2 describes the data, the atmospheric model, and analysis methods that we use in this study. Section 3 presents the climatology and intraseasonal variability of the simulated near-surface air temperature, the WACNA pattern and its temporal evolution. Section 4 examines the dynamical processes associated with the generation of WACNA. Specifically, the role of the time-mean flow and contribution of synoptic-scale transient eddies are analyzed. A summary and discussion are given in section 5.

2. Data and the model

For the observational analysis, we make use of the European Centre for Medium-Range Weather Forecasts (ECMWF) interim reanalysis (ERA-Interim; Dee et al. 2011). Variables analyzed include 2-m air temperature (T2m), 950-hPa temperature (T950), 250-hPa zonal and meridional winds (u250 and v250), and 500- and 250-hPa geopotential heights (Z500 and Z250). The original data are four times daily on a $0.75° \times 0.75°$ resolution. The analysis is performed with the daily average and the data are interpolated to a $2.5° \times 2.5°$ resolution. For the analysis of intraseasonal variability, the data are averaged over nonoverlapping 5-day periods (pentads). The analysis is conducted for 40 extended winters from 1979/80 to 2018/19, where the extended winter is defined as the 30 pentads starting from the pentad of 2–6 November and ending at the pentad of 27–31 March. For leap years, the pentad of 25 February to 1 March has 6 days. To obtain the anomaly, the 40-yr climatology of each pentad is first removed at each grid point. The mean of each extended winter is then removed in order to filter out the interannual variability.

We make use of the SGCM which is described in Hall (2000) and used in a number of previous studies (e.g., Hall et al. 2001; Lin et al. 2007, 2010). Based on the primitive equation model of Hoskins and Simmons (1975), it is a global spectral model with a horizontal resolution of T31. The model has 10 vertical levels ranging from 50 to 950 hPa at an interval of 100 hPa. Equations of vorticity, divergence, surface pressure, and temperature are integrated in the model with a scale-selective dissipation and a level-dependent linear damping on temperature and momentum. It is a dry model with no moisture representation. An important aspect of this model is that a time-independent forcing is used that is calculated empirically from the observational daily data. This forcing is computed as a residual for each tendency equation, including dynamical terms and dissipation, with daily global analyses and average in time. Details of the forcing calculation can be found in Hall (2000). All the processes that are not resolved by the model's dynamics are included in the forcing. No topography is prescribed in the model, but its time-mean effect is accounted for by the forcing. This SGCM model is found to reproduce reasonably well the observed climatology and response to specified thermal forcing (e.g., Hall 2000; Hall et al. 2001; Lin et al. 2007, 2010). In this study, the daily data of the ERA-Interim for the extended winters (1 November–31 March) of 1979/80–2018/19 are used to calculate the forcing fields. With this time-independent climatological forcing, a perpetual extended boreal winter integration of 7300 days is conducted starting from an observed initial condition. Daily output is saved and interpolated to a $2.5° \times 2.5°$ resolution for analysis. The first 100 days are taken as a spinup of the model and are not used. The remaining 7200 days of data are grouped as pentad averages with a total of 1440 pentads, and pentad anomalies are obtained by subtracting the time mean.

With the pentad temperature anomaly of the ERA-Interim and the SGCM simulation, separate empirical orthogonal function (EOF) analyses over the North American/North Pacific sector are performed to identify the leading modes of intraseasonal surface air temperature variability in the observation and the model. As will be seen, EOF1 corresponds to the WACNA pattern. We then use the principal component of EOF1 (PC1) as an index of this pattern, and analyze lead–lag associations with variables of interest. Statistical significance is assessed using a Student's t test where the effective degrees of freedom are estimated taking into account the autocorrelation of the time series (Bretherton et al. 1999). To avoid possible over interpretation of multiple testing results for grid points over the Northern Hemisphere domain, the approach of false detection rate (FDR) as described in Wilks (2016) is applied.

To analyze how the circulation anomalies lead to the WACNA temperature anomaly, as in Yu and Lin (2019), horizontal temperature advection in the lower troposphere is calculated as

$$F_{\text{adv}} = -u^* \frac{\partial \overline{T}}{\partial x} - v^* \frac{\partial \overline{T}}{\partial y}, \tag{1}$$

where u^* and v^* denote the anomalous zonal and meridional wind components derived from a WACNA related composite, and $\overline{T}$ the extended winter climatological mean temperature.

To understand the dynamics of atmospheric variability on the intraseasonal time scale, we analyze its interactions with the time-mean flow and synoptic-scale transients. Let us write an atmospheric variable Z as three parts: $Z = \overline{Z} + Z^* + Z'$, where $\overline{Z}$ is the climatological time-mean flow, Z^* the low-frequency (or intraseasonal) variability part, and Z' the high-frequency (or synoptic-scale) component. The low-frequency variability interacts with both the mean flow $\overline{Z}$, and the high-frequency variability Z'.

On the interaction with the mean flow, we look at the kinetic energy exchange. Following Simmons et al. (1983), the growth of kinetic energy (KE) of low-frequency eddies through barotropic energy exchange with the basic state, can be approximated as

$$\frac{\partial \mathrm{KE}}{\partial t} = \mathrm{CK}x + \mathrm{CK}y, \tag{2}$$

where

$$\mathrm{CK}x = -(u^{*2} - v^{*2})\frac{\partial \overline{U}}{\partial x} \quad \text{and} \quad Ky = -u^* v^* \frac{\partial \overline{U}}{\partial y},$$

with $\overline{U}$ the zonal wind of the time-mean basic state and u^* and v^* the intraseasonal zonal and meridional winds associated with WACNA, respectively. CKx and CKy are associated with the zonal and meridional gradients of the basic-state zonal wind.

To analyze Rossby wave propagation, the stationary wavenumber (Ks) is defined, following Hoskins and Ambrizzi (1993), as

$$\mathrm{Ks} = \left(\frac{\overline{\zeta}_\varphi}{\overline{U}}\right)^{1/2} a\cos\varphi, \tag{3}$$

where $\overline{\zeta}_\varphi$ is the meridional gradient of the time-mean absolute vorticity, a Earth's radius.

To diagnose wave activity flux, the **W** vector defined by Takaya and Nakamura (2001) is used. The horizontal components of the **W** vector are given by

$$\mathbf{W} = \frac{1}{2|\overline{\mathbf{U}}|}\begin{bmatrix} \overline{U}(\psi_x^{*2} - \psi\psi_{xx}^*) + \overline{V}(\psi_x^*\psi_y^* - \psi^*\psi_{xy}^*) \\ \overline{U}(\psi_x^*\psi_y^* - \psi^*\psi_{xy}^*) + \overline{V}(\psi_y^{*2} - \psi^*\psi_{yy}^*) \end{bmatrix}, \tag{4}$$

where the subscripts denote partial derivatives, $\overline{\mathbf{U}} = (\overline{U}, \overline{V})$ is the basic-state wind vector, and ψ^* the intraseasonal perturbation streamfunction associated with WACNA. The **W** vector is parallel to the local group velocity of stationary Rossby waves for a slowly varying background flow.

To analyze the interaction between WACNA and the high-frequency eddies, we look at the vorticity flux convergence by the synoptic-scale transient eddies. The vorticity tendency can be expressed as a geopotential height tendency by taking an inverse Laplacian, which has the effect of spatial smoothing (e.g., Hoskins et al. 1983; Lau 1988); thus,

$$\frac{\partial \tilde{Z}}{\partial t} = \frac{f}{g}\nabla^{-2}[-\nabla \cdot \widetilde{\mathbf{V}'\zeta'}], \tag{5}$$

where the prime represents the synoptic transients, and the tilde is time average over a pentad. ζ is the relative vorticity, **V** the wind velocity, g the acceleration due to gravity, and f the Coriolis parameter. In practice, the synoptic eddy component is the departure of daily data from the pentad mean.

3. Simulated near-surface air temperature

a. Climatology

The extended boreal winter climatology of the ERA-Interim is in general well simulated by the SGCM integration. Shown in Figs. 1a and 1b are the time-mean zonal winds at 250 hPa ($\overline{\mathrm{U}}250$). We start by looking at the general features of the temperature climatology and intraseasonal variability at 950 hPa, which is the lowest model level of SGCM. The observed 40-yr average of temperature for the extended winter (NDJFM) (Fig. 1c) is well simulated by the long perpetual extended winter SGCM integration (Fig. 1d). Strong meridional gradients of climatological T950 are found in the midlatitude Eurasian and North American continents, as well as along the storm-track regions in the North Pacific and North Atlantic (Figs. 1e,f). In the high latitudes, two zonally elongated regions of strong T950 gradient are seen, one from eastern Russia across the Bering Strait to Alaska and Canada, and the other from Greenland to the Barents Sea. They are associated with the strong temperature contrast between the cold Arctic and the oceans.

The strength of intraseasonal variability is assessed by the standard deviation of pentad T950 in the extended winter which is shown is Figs. 1g and 1h for the observations and SGCM simulation, respectively. In the observations, strong intraseasonal temperature variability is found over the mid- and high-latitude land regions, consistent with previous studies (e.g., Guan et al. 2020b). The spatial distribution of the simulated intraseasonal variability is generally similar to the observations. The main difference is seen in the central Siberian region and north of Alaska, where the SGCM fails to reproduce the strong observed temperature variability. It is likely that this observed temperature variability in these places is associated with variations in local snow cover (e.g., Yu and Lin 2022) and sea ice, which are absent in the SGCM. By comparing with Figs. 1e and 1f, it appears that strong intraseasonal temperature variability is associated with a strong mean meridional temperature gradient, suggesting that atmospheric internal dynamics or instability related to this temperature gradient is largely responsible for the generation of the intraseasonal temperature variability. For some variables, the magnitude of high-frequency transient variability simulated by the SGCM is weaker than the observed. As discussed in Hall (2000), although the Northern Hemisphere total transient-eddy fluxes of temperature at low levels and momentum at upper levels are well simulated by the SGCM model in both position and magnitude, the total transient-eddy kinetic energy is only half of what it should be. This discrepancy may be associated with the simplified model physics, e.g., orography and nonlinearity in the representation of drag and diffusion. The SGCM also lacks variability in the external forcing that exists in the real world,

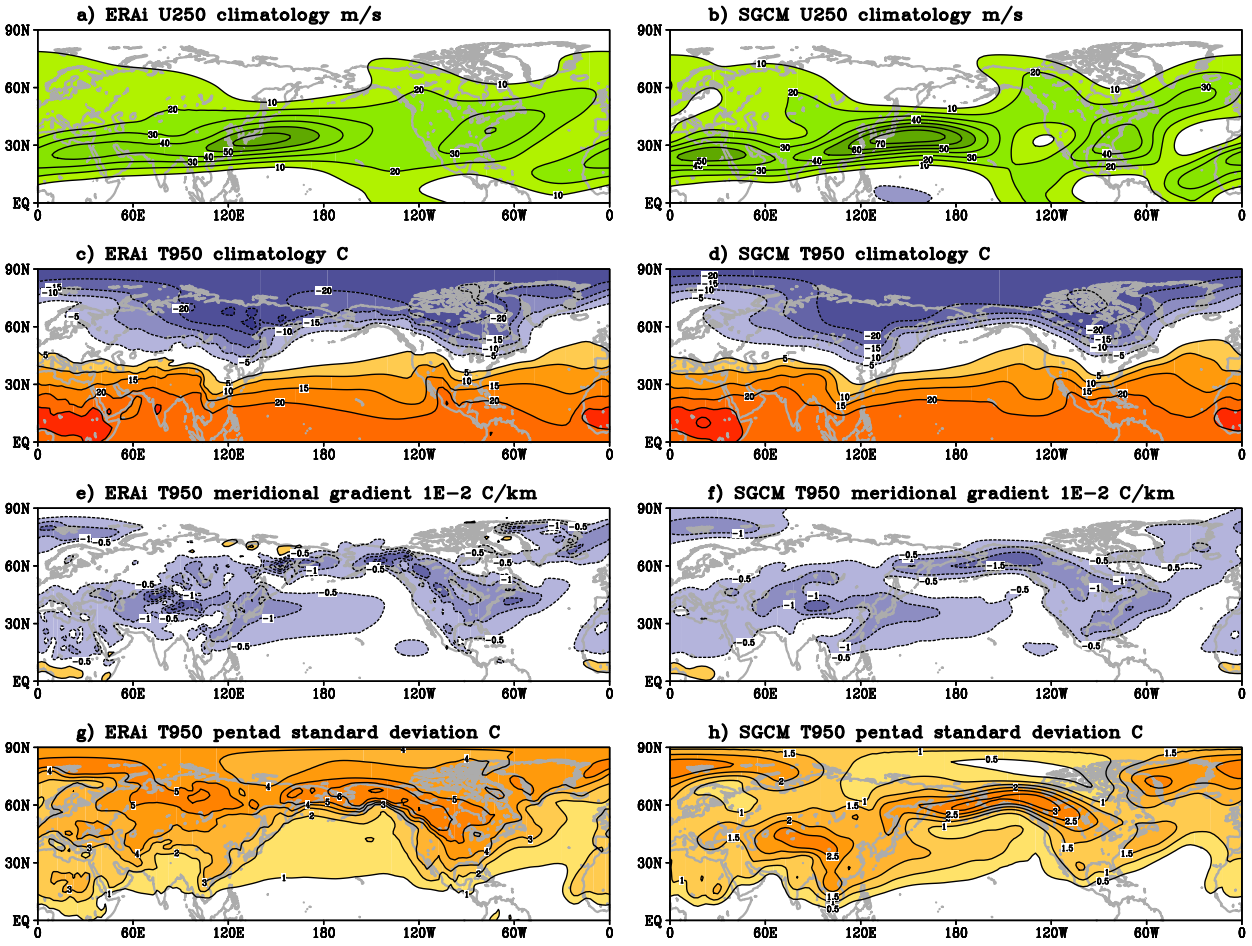

FIG. 1. (a),(b) Time-mean zonal wind at 250 hPa (U250) in extended boreal winter. (c),(d) Time-mean temperature at 950 hPa (T950). (e),(f) Meridional gradient of the time-mean T950. (g),(h) Standard deviation of pentad T950. (left) ERA-Interim and (right) SGCM simulation. The contour interval is 10 m s^{-1} for (a) and (b), 5°C for (c) and (d), 0.5 × 10^{-2} °C km^{-1} for (e) and (f), 1°C for (g), and 0.5°C for (h). Contours with negative values are dashed. The zero contour is omitted.

e.g., variability in SST, sea ice, land surface, and tropical diabatic heating, as well as coupling with moist thermodynamic processes and with the stratosphere (e.g., Domeisen and Butler 2020), potentially accounting for weaker simulated variability than in the observations. The observed climatology and intraseasonal variability of T2m are very similar to those of T950 (not shown).

b. *The leading modes of intraseasonal temperature variability*

With the observed pentad T2m anomaly, EOF analysis is performed over the region of 20°–90°N, 150°E–40°W. The T2m anomaly is area weighted by multiplying the data by the square root of cosine of the latitude before the EOF analysis. We have repeated the calculation with the observed T950 anomaly and found almost identical results. The temporal correlation between T2m PC1 and T950 PC1 is 0.99. Therefore, in the following discussion we use the T2m EOF results for the observation. The same procedure is applied to the simulated pentad T950 anomaly to get the leading modes of intraseasonal temperature variability in the SGCM.

Shown in Figs. 2a and 2b are EOF1 and EOF2 of the observed T2m, which account for 24% and 14% of the total variance, respectively. Very similar two leading modes of pentad T2m were obtained using the National Centers for Environmental Prediction–National Center for Atmospheric Research (NCEP–NCAR) reanalysis data (Kalnay et al. 1996) over the North American region (e.g., Lin 2015). EOF1 is characterized by a dipole pattern of T2m anomalies with one center in the polar region near the Chukchi and Bering Seas and the other center of opposite sign over North America. This pattern is highly similar to the WACC pattern over the North American sector, i.e., WACNA, as observed in surface air temperature trend (e.g., Sigmond and Fyfe 2016; Cohen et al. 2021), interannual (e.g., Kug et al. 2015; Yu and Lin 2022), and intraseasonal variations (e.g., Lin 2015, 2018; Guan et al. 2020a,b). EOF2 features a temperature variability center over Alaska, and two relatively weak centers with opposite sign, one over eastern Siberia and the other in southeast North America.

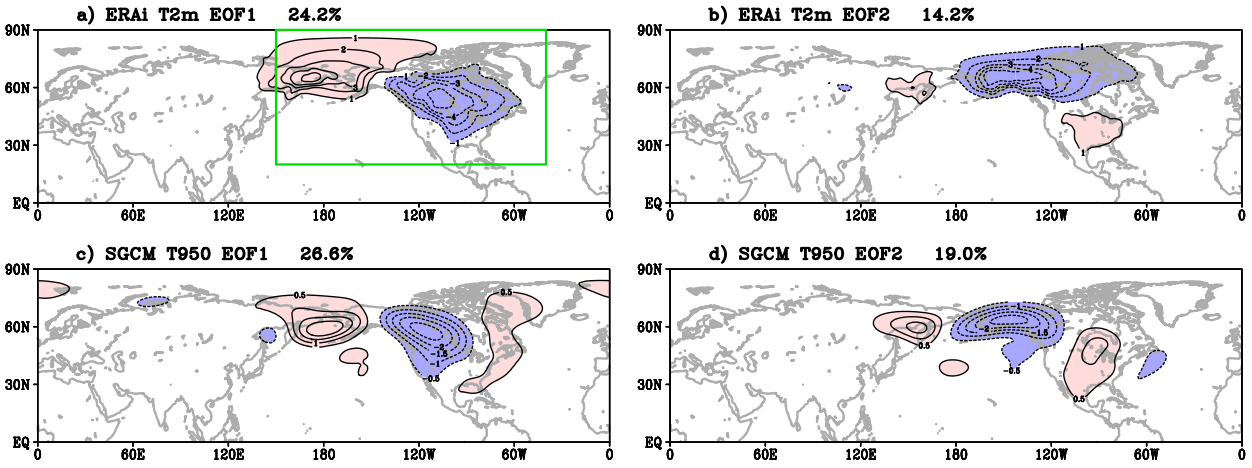

FIG. 2. (a) EOF1 and (b) EOF2 of T2m of ERA-Interim represented as regressions of pentad T2m onto PC1 and PC2, respectively. (c),(d) As in (a) and (b), but for the SGCM simulated T950. The magnitude corresponds to one standard deviation of the corresponding PC. The contour interval is 1°C for (a) and (b), and 0.5°C for (c) and (d). Contours with negative values are dashed. The zero contour is not plotted. The percentage of variance explained by each EOF mode is indicated above each panel. The green box in (a) indicates the region for the EOF analysis.

EOF analysis of the SGCM simulated pentad T950 reveals that the model can generate two leading modes of variability that match those of the observed T2m remarkably well (Figs. 2c,d). EOF1 and EOF2 account for 27% and 19% of the total variance, respectively, similar to their observational counterparts. As in the observations, the simulated EOF1 closely resembles the WACNA pattern. Power spectrum analysis of PC1 indicates that both the observed and simulated PC1 have a spectrum peak near five pentads (25 days) (Fig. 3). Autocorrelation of PC1 is also calculated, which shows an *e*-folding time scale consistent with the power spectrum analysis. This implies that the WACNA is an important mode of intraseasonal variability and is relevant for subseasonal predictions of surface temperature. There are some spectral peaks at lower frequencies that are different between the observations and the model. This is likely related to variabilities in boundary forcing in the observations, e.g., SST, sea ice, and snow cover, that are absent in the SGCM. It is also possible that the perpetual model run can internally generate some slow variability different from the observations. The model EOF1 tends to vary more slowly than the observations.

To see the evolution of the WACNA pattern, lead–lag regressions of the observed anomalous T2m with respect to the observed PC1 are calculated, which are compared with the lead–lag regressions of the SGCM simulated T950 anomalies with respect to its PC1. Shown in Fig. 4 are the regressions from lag = −3 pentads to lag = −1 pentad, where the negative lag indicates that the temperature anomaly leads PC1. About

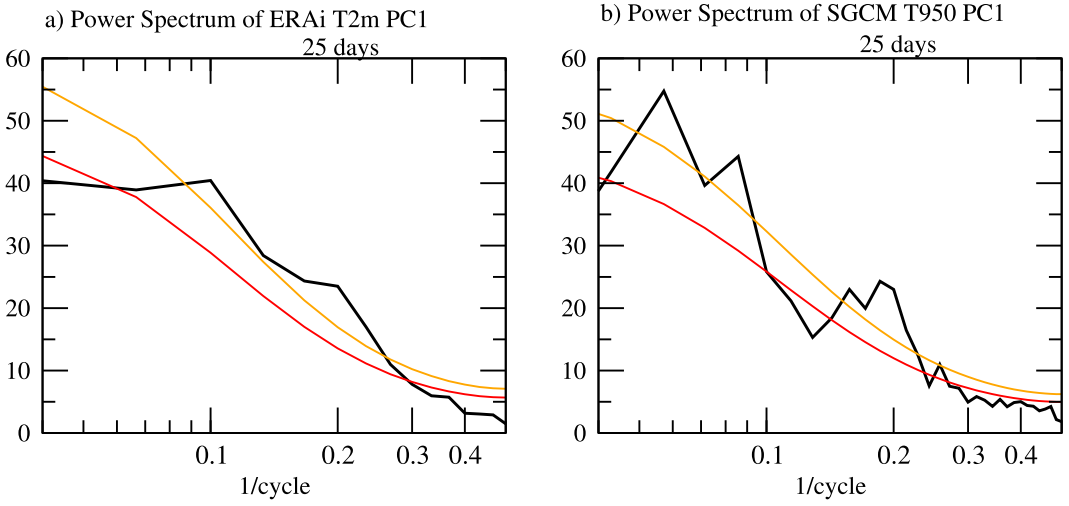

FIG. 3. Power spectra of PC1 for (a) ERA-Interim T2m and (b) SGCM simulated T950. The red curve is the red-noise spectrum computed from the lag-1 autocorrelation, and the orange curve is for the 0.05 significance level.

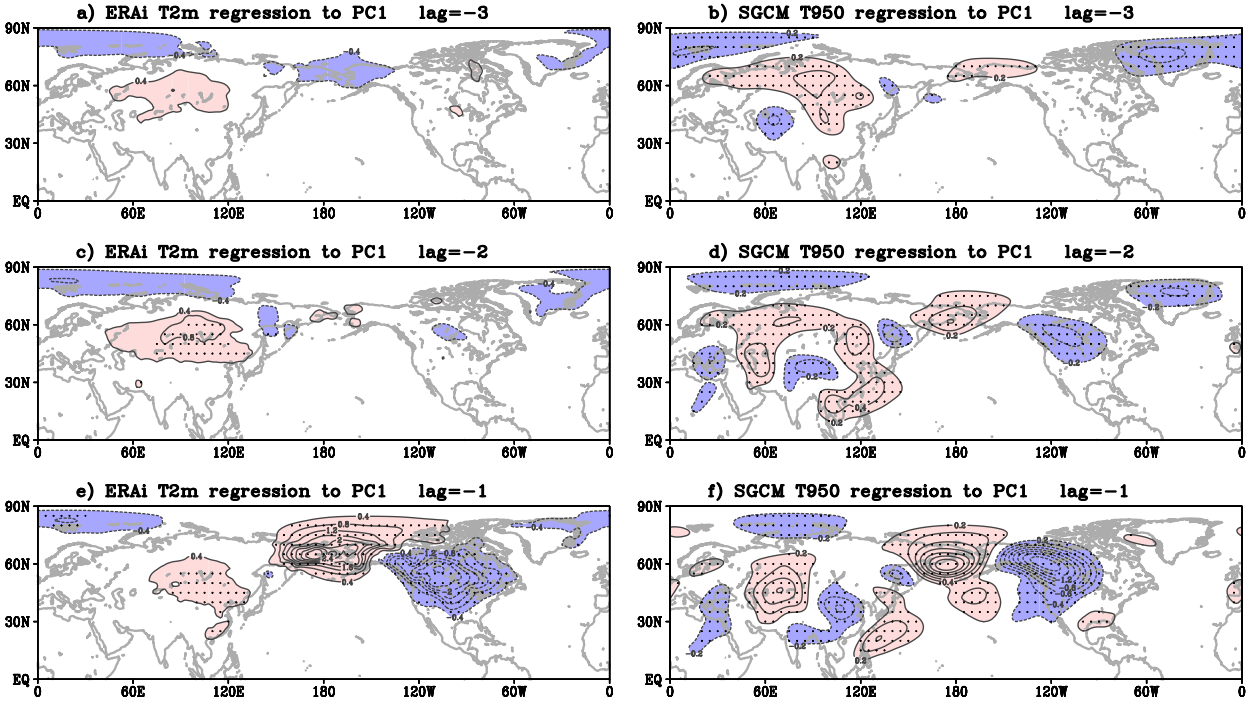

FIG. 4. (left) Lead–lag regressions of T2m onto PC1 for the ERA-Interim. (right) Lead–lag regressions of T950 onto PC1 for the SGCM simulation. Lag = $-n$ means that the temperature anomaly leads PC1 by n pentads. The contour interval is 0.4°C for the left panels and 0.2°C for the right panels. Contours with negative values are dashed. The zero contour is omitted. Areas with dots indicate that the regression is statistically significant with p values small enough to satisfy the FDR criterion of $\alpha_{FDR} = 0.05$ (Wilks 2016).

three pentads preceding a positive WACNA, negative temperature anomalies are found in the polar region near the Barents–Kara Seas, and positive temperature anomalies appear in the southern Siberian region. This resembles the negative phase of the WACE pattern (e.g., Mori et al. 2014; Sun et al. 2016). Similar lagged connection between WACE and WACNA was found in Lin (2018) and was recently reported on a seasonal time scale (Yu and Lin 2022). The WACNA evolution in the SGCM simulation (right panels of Fig. 4) is in general similar to the observation. At lag = −2 and lag = −1, the regressions of the simulated T950 anomaly show smaller-scale zonally oriented wave train features in the East Asian midlatitude and subtropical regions (Figs. 4d,f), which is related to the waveguide effect of the jets, as will be discussed in the next section.

Figure 5 shows the evolution of the Z250 anomaly associated with WACNA in the ERA-Interim and the SGCM simulation. At lag = 0, WACNA is associated with positive Z250 anomalies in the polar region centered near the North Pacific–Bering Sea region, and negative Z250 anomalies over North America. Two to three pentads before, negative Z250 anomalies are observed in the polar region centered near the Barents Sea, with positive Z250 anomalies over the southern Siberian area, associated with the negative WACE. Similar connection between the WACNA and WACE was observed in Yu and Lin (2022). In the high latitudes from eastern Siberia across the Bering Sea to North America, the pattern bears some similarity to the Asian–Bering–North American (ABNA) teleconnection as described in Yu et al. (2018). In the North Pacific–North American sector, the Z250 anomaly distribution resembles the negative phase of the Pacific–North American pattern (PNA; e.g., Wallace and Gutzler 1981). There are also some similarities with the Alaskan Ridge weather regime as observed in previous studies (e.g., Straus et al. 2007; Vigaud, et al. 2018; Lee et al. 2019). The geopotential height anomalies have an equivalent barotropic vertical structure in the upper troposphere, with the distribution at the 250-hPa level very similar to that at 500 hPa (not shown). Again, SGCM is able to reproduce the observed features.

The evolution of WACNA temperature anomalies in Fig. 4 is closely associated with that of the circulation anomalies. In the lower troposphere, circulation anomalies induce horizontal temperature advection, resulting in temperature anomalies. Shown in Fig. 6 is temperature advection at 850 hPa (F_{adv}) calculated according to (1). At lags −1 and 0, warm and cold temperature advection occurs over the Chukchi and Bering Sea region and western North America, respectively, indicating that the lower-tropospheric horizontal temperature advection largely contribute to the development and maintenance of the WACNA temperature pattern. This result is similar to previous studies (e.g., Clark and Lee 2019; Yu and Lin 2019; Park and Lee 2021) that documented the role of temperature advection in other large-scale temperature anomaly patterns. The lower-tropospheric temperature advection is dominated by that due to the meridional wind component (not shown).

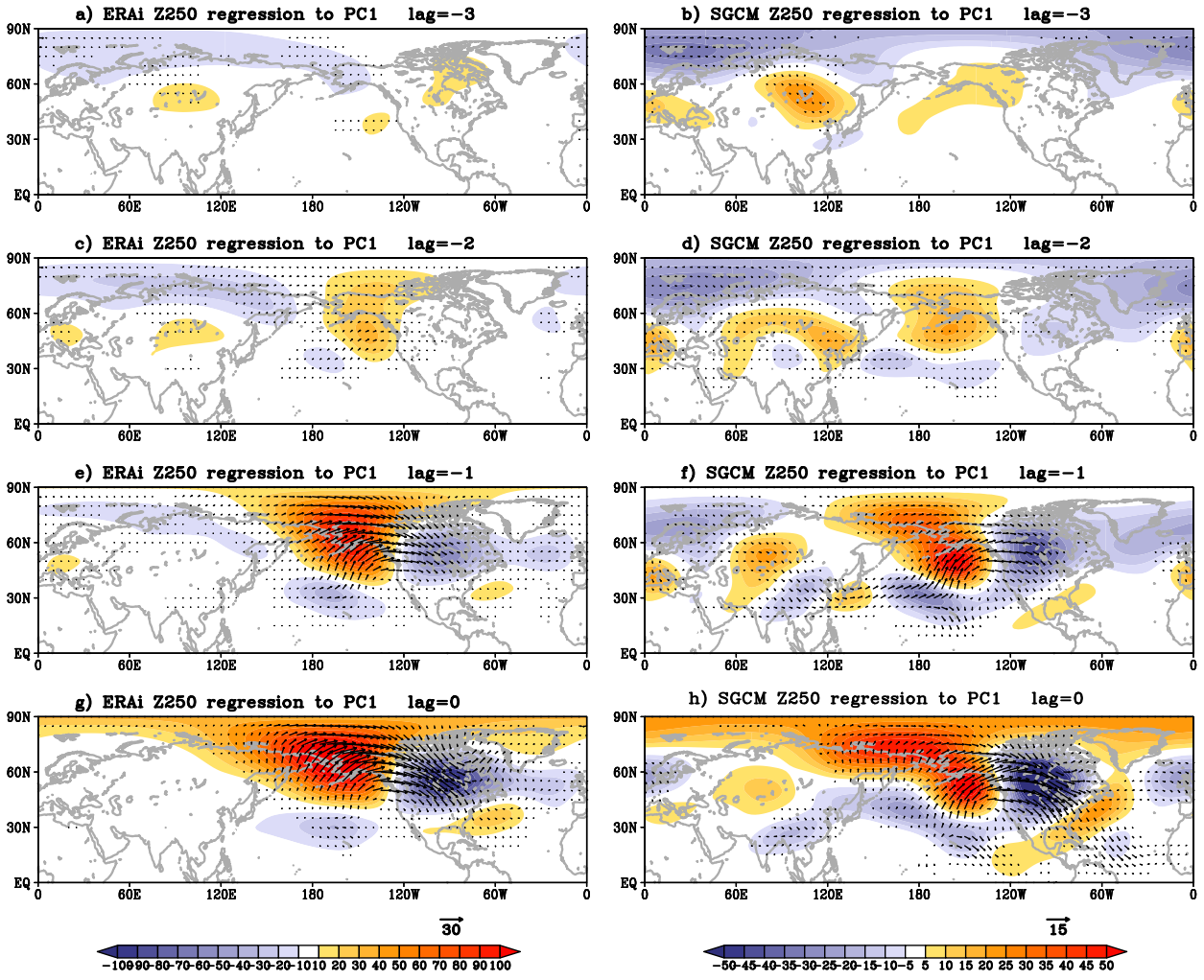

FIG. 5. Lead–lag regressions of Z250 against PC1 (color; in m; scale at the bottom) and associated wave activity flux (arrows) for the (left) ERA-Interim and (right) SGCM simulation. Vector scale (in $m^2\ s^{-2}$) is indicated at the bottom right of each column, and vectors with magnitude less than $0.2\ m^2\ s^{-2}$ are not displayed.

In summary, the SGCM model simulates well the behavior of the WACNA pattern. We emphasize that the SGCM only has a time-independent forcing with very limited representation of the stratosphere. The above results clearly demonstrate that the tropospheric internal dynamics alone is able to generate the WACNA pattern.

4. Dynamical processes

a. Role of the mean flow

In this subsection, we analyze the interaction between the WACNA related low-frequency variability and the time-mean flow. One energy source for the low-frequency variability is the barotropic energy exchange with the background mean flow. As shown in Figs. 1a and 1b for the time-mean zonal winds at 250 hPa ($\overline{U}250$) in extended boreal winter for the ERA-Interim and the SGCM simulation, familiar features are seen such as the subtropical westerly jets with maximum zonal winds in the western North Pacific and western North Atlantic. In the high latitudes around 60°N, relatively weak $\overline{U}250$ appears near the eastern Siberia and Bering Strait region, in contrast to the relatively strong zonal wind to the east, thus forming a positive zonal gradient of U250 near Alaska.

We calculate CKx and CKy of (2) with u^* and v^* as those obtained from the lead–lag regressions of 250-hPa winds with respect to PC1, and then average from lag = −2 to lag = +2 pentads, which covers about one life cycle of WACNA. Figures 7a and 7b are CKx for the ERA-Interim and SGCM, respectively. Over the region near Alaska, we see kinetic energy conversion from the mean flow to the WACNA pattern in both the observation and the SGCM simulation. Collocated with $\partial\overline{U}/\partial x > 0$, the perturbed meridional wind there is stronger than the zonal wind on the east side of the north center of WACNA (see Fig. 5); thus, $u^{*2} - u^{*2} < 0$, resulting in CK$x > 0$. Positive CKx is also seen in the midlatitude

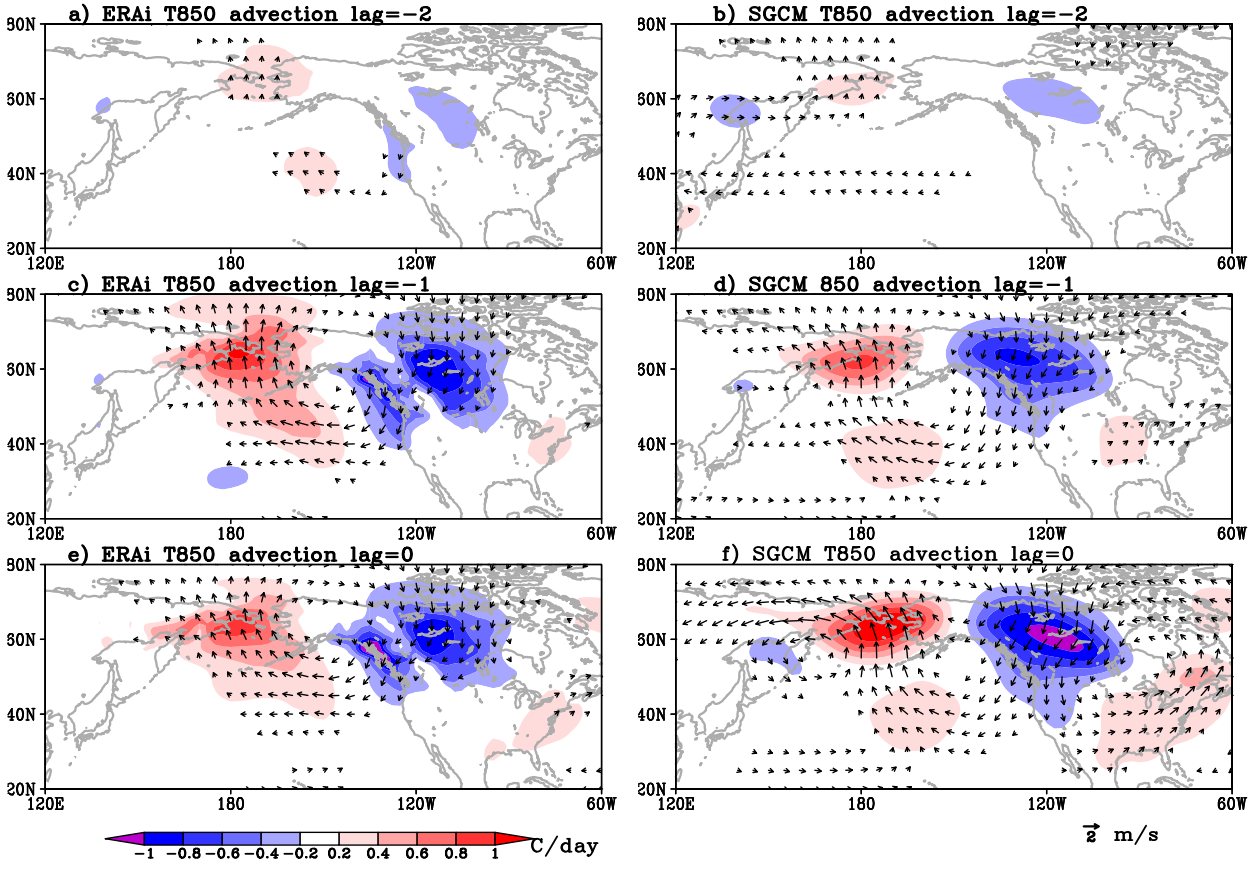

FIG. 6. Anomalies of temperature advection (in color) and winds (in arrows) at 850 hPa associated with PC1 for (left) ERA-Interim and (right) SGCM. Lag = $-n$ means that the anomalies lead PC1 by n pentads. Anomalous winds with a speed less than 0.5 m s^{-1} are omitted.

central North Pacific, which is associated with the subtropical jet exit ($\partial\overline{U}/\partial x < 0$) at the southern flank of the Chukchi and Bering Sea WACNA center where $u^{*2} - v^{*2} > 0$. This positive CKx in the central North Pacific is consistent with previous studies (e.g., Simmons et al. 1983). For CKy (Figs. 7c,d), positive values are observed in the region to the northeast of Alaska/northwest Canada, which may also contribute to WACNA. Positive and negative CKy can be seen in the North Pacific on the south and north sides of the jet, respectively, which is associated with the northwest–southeast orientation of perturbed wind where $u^*v^* < 0$. In the SGCM simulation (Fig. 7d), some small-scale features of CKy are also observed along the subtropical jet across Eurasia. The sum of CKx and CKy is shown in Figs. 7e and 7f for the observations and SGCM.

Rossby wave propagation in the extratropical atmosphere is largely determined by the structure of the basic-state zonal wind. Plotted in Fig. 8 (in color) is the stationary wavenumber, Ks, as defined in (3) at 250 hPa for the ERA-Interim (Fig. 8a) and the SGCM simulation (Fig. 8b) in the extended boreal winter. The general features seen in the ERA-Interim are consistent with previous studies for boreal winter (e.g., Henderson et al. 2017; Soulard et al. 2021). Ks is undefined and wave propagation does not occur in the gray color regions where the basic-state zonal wind becomes zero or easterly ($\overline{U} \le 0$). Areas with white color indicate that the meridional gradient of absolute vorticity ($\overline{\zeta}_\varphi$) is negative, where continuous wave propagation is not permitted. Stationary Rossby waves are reflected toward larger Ks values. The midlatitude strong westerly jet acts as a waveguide where Ks is maximum. Less often discussed in previous studies are the high-latitude regions near the polar jet stream where there are two regions of large Ks, one over Eurasia along about 60°N, which is connected with the midlatitude waveguide across the North Atlantic, and the other from northeastern Siberia across the Bering Strait to Canada, which then merges with the midlatitude waveguide over North America. The high-latitude Ks is smaller than that in the subtropical jets, but still allows longer waves to propagate. It is likely that the high-latitude waveguide connecting Siberia and North America plays an important role for the circulation pattern associated with WACNA. The SGCM simulation reproduces the observed stationary wavenumber reasonably well (Fig. 8b).

We calculate the **W** vector defined in (4) at 250 hPa associated with WACNA using ψ^* as the lead–lag regressions of streamfunction with respect to PC1, and plot it in Fig. 5 as arrows. It is also shown in Fig. 8 in arrows for lag = −1 when the streamfunction anomaly leads PC1 by one pentad. Wave

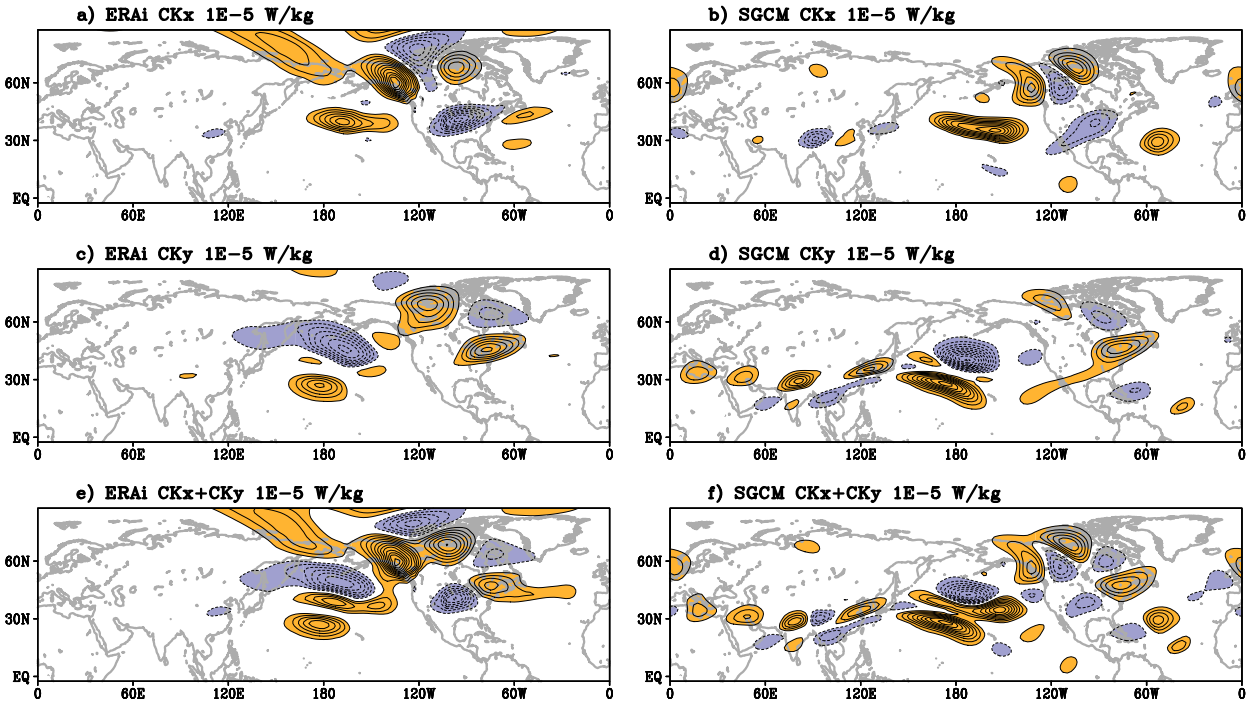

FIG. 7. (top) Kinetic energy conversion associated with zonal gradient of the time-mean zonal wind (CKx). (middle) Kinetic energy conversion associated with meridional gradient of the time-mean zonal wind (CKy). (bottom) Sum of CKx and CKy. (left) ERA-Interim and (right) SGCM simulation. The contour interval is 1×10^{-5} W kg^{-1}. Contours with negative values are dashed. The zero contour is omitted.

activity flux tends to follow the waveguides. In both the observations and the SGCM simulation, it is clear that wave activity fluxes of two origins influence North America, one from eastern Siberia across the Bering Sea and Strait (north pathway), and the other from the subtropical North Pacific across the eastern North Pacific (subtropical pathway). Therefore, wave propagation and wave activity flux along these two pathways contribute to the formation of the WACNA. Similar result was reported in Yu and Lin (2022) in the analysis of interannual variability of the WACNA pattern. Previous studies found similar pattern for atmospheric disturbances propagating along the north pathway to influence North America, i.e., the ABNA teleconnection (e.g., Yu and Lin 2018; Yu et al. 2018). Although there is some indication in the observations that the Siberian snow-cover variability may contribute to the wave activity in the north pathway (e.g., Yu and Lin 2019, 2022) and the subtropical pathway may be connected to tropical convection anomalies associated with ENSO and MJO (e.g., Lin 2015; Guan et al. 2020b; Yu and Lin 2022), a considerable part of the wave activity can be attributed to the atmospheric internal dynamics, as is evidenced by the SGCM simulation. It is possible that waves internally generated by the positive CKx and CKy in the central North Pacific as observed in Fig. 7 will propagate along the subtropical pathway to influence the WACNA.

b. *Contribution of the synoptic transient eddies*

The intraseasonal variability of WACNA interacts not only with the time-mean flow, but also with the high-frequency synoptic transients. The barotropic feedback of the synoptic-scale transient eddies onto WACNA is analyzed in this subsection.

Our calculation for the geopotential height tendency is performed at 250 hPa for each pentad using (5), with the tilde representing the pentad average and the prime departure of daily data from the pentad mean. Lead–lag regressions of the pentad geopotential height tendency with respect to PC1 are then calculated and presented in Fig. 9, which illustrates the feedback of the synoptic-scale transient eddies onto the intraseasonal circulation associated with the WACNA pattern. Comparing with the Z250 anomaly (Fig. 5), we see that the centers of the eddy feedback match those of the geopotential height anomaly for both the observation and the SGCM simulation, indicating that the eddy feedback contributes constructively to the wave train centers in the mid–high latitudes. The eddy feedback in the observation is more confined to the North Pacific and WACNA sector, while in the SGCM simulation it occurs over a wide area of the Northern Hemisphere. At lag = 0, the tendency in the SGCM is located primarily the North Atlantic region (Fig. 9h). Corresponding to the major positive center of WACNA near Alaska, the eddy feedback appears to be the strongest when leading PC1 by one pentad (lag = −1, Figs. 9e,f), implying that the eddy feedback acts as a forcing to the intraseasonal variability of WACNA, which is clearer in the SGCM simulation than the observation. The maximum magnitude of this feedback is about 10 m day^{-1} for the observation and 5 m day^{-1} for SGCM, suggesting that it would take about 10 days to establish the WACNA Z250

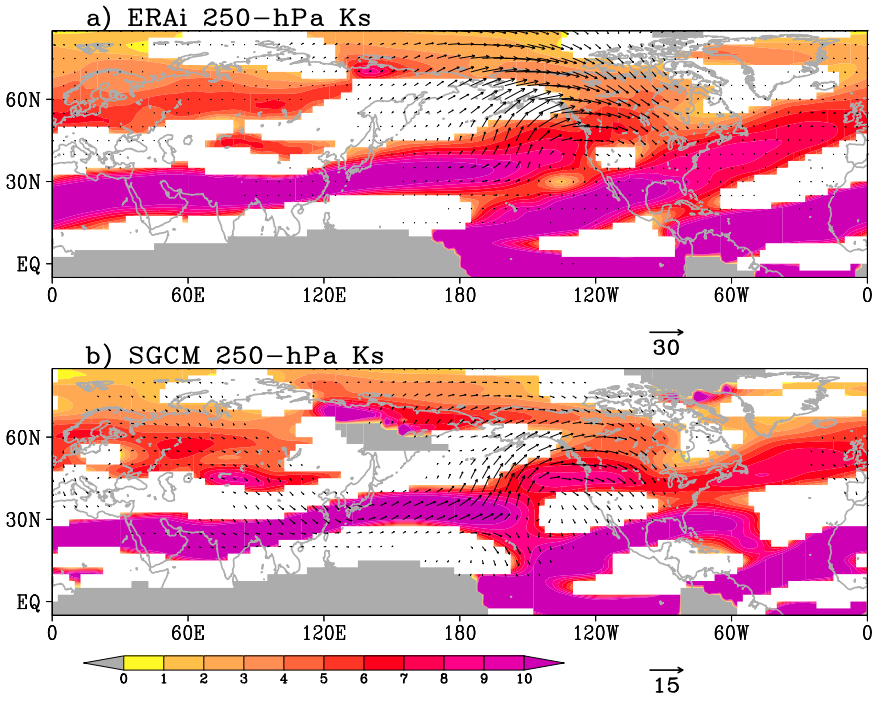

FIG. 8. Stationary Rossby wavenumber Ks at 250 hPa during extended boreal winter for (a) ERA-Interim and (b) SGCM simulation. Gray shading indicates where the time-mean zonal wind is easterly, and white shading where the meridional gradient of the mean absolute vorticity is negative. Wave activity flux (**W**) of lag = −1 pentad with respect to PC1 is plotted in vectors. Vector scale (in $m^2\ s^{-2}$) is indicated at the bottom right of each panel, and vectors with magnitude less than 0.2 $m^2\ s^{-2}$ are not displayed.

anomaly pattern (see Fig. 5) if the feedback of synoptic-scale eddies is the only forcing.

5. Summary and discussion

The WACC pattern is of great interest because it connects atmospheric and sea ice conditions in the northern polar region with weather and climate over the midlatitude continents, and thus implies a potential impact of Arctic amplification and global warming. There has been some debate as to whether the WACC pattern is driven by external forcing such as sea ice variability or is generated by atmospheric internal dynamics. In this study, we have examined the driving mechanisms for the WACC pattern in the North American sector, WACNA, using a simple primitive equation model (SGCM). Since the model atmosphere is maintained by a time-independent forcing, the contribution of atmospheric internal dynamics can be studied independently of any influence from external forcing.

The SGCM is able to simulate reasonably well the observed temperature climatology and intraseasonal variability. EOF analysis of the pentad averaged 950-hPa temperature from a long perpetual extended boreal winter integration of SGCM reveals that the leading mode (EOF1) reproduces the observed WACNA pattern. The simulated evolution of 950-hPa temperature as well as 250-hPa geopotential height associated with WACNA is also similar to the observations. In both observations and SGCM simulation, the positive phase of the intraseasonal WACNA variability is led by a negative phase WACE, i.e., a warm Arctic–cold Eurasia pattern, by about 15 days. This result confirms that tropospheric internal dynamics alone is able to generate the WACNA pattern.

The structure of the time-mean flow plays a key role in the intraseasonal variability and the WACNA pattern. Strong intraseasonal temperature variance is largely collocated with strong mean meridional temperature gradients over the midlatitude continental regions and in two high-latitude zones: one extending from eastern Siberia across the Bering Strait to Canada, and the other from Greenland to the Barents Sea. In the upper troposphere, barotropic kinetic energy conversion from the mean flow to the WACNA circulation occurs near the Bering Strait/Alaska region, which is associated with the local zonal gradient of the mean flow zonal wind. The basic-state zonal wind also determines the Rossby wave propagation. Stationary wavenumber analysis shows that in addition to the subtropical waveguide there is a high-latitude region of large Ks extending from northeastern Siberia across the Bering Strait to Canada. Wave activity flux originating from eastern Siberia propagates eastward across the Bering Strait, and joins with that from the subtropical North Pacific to influence North America, leading to the development of WACNA. In addition, the WACNA circulation also interacts with

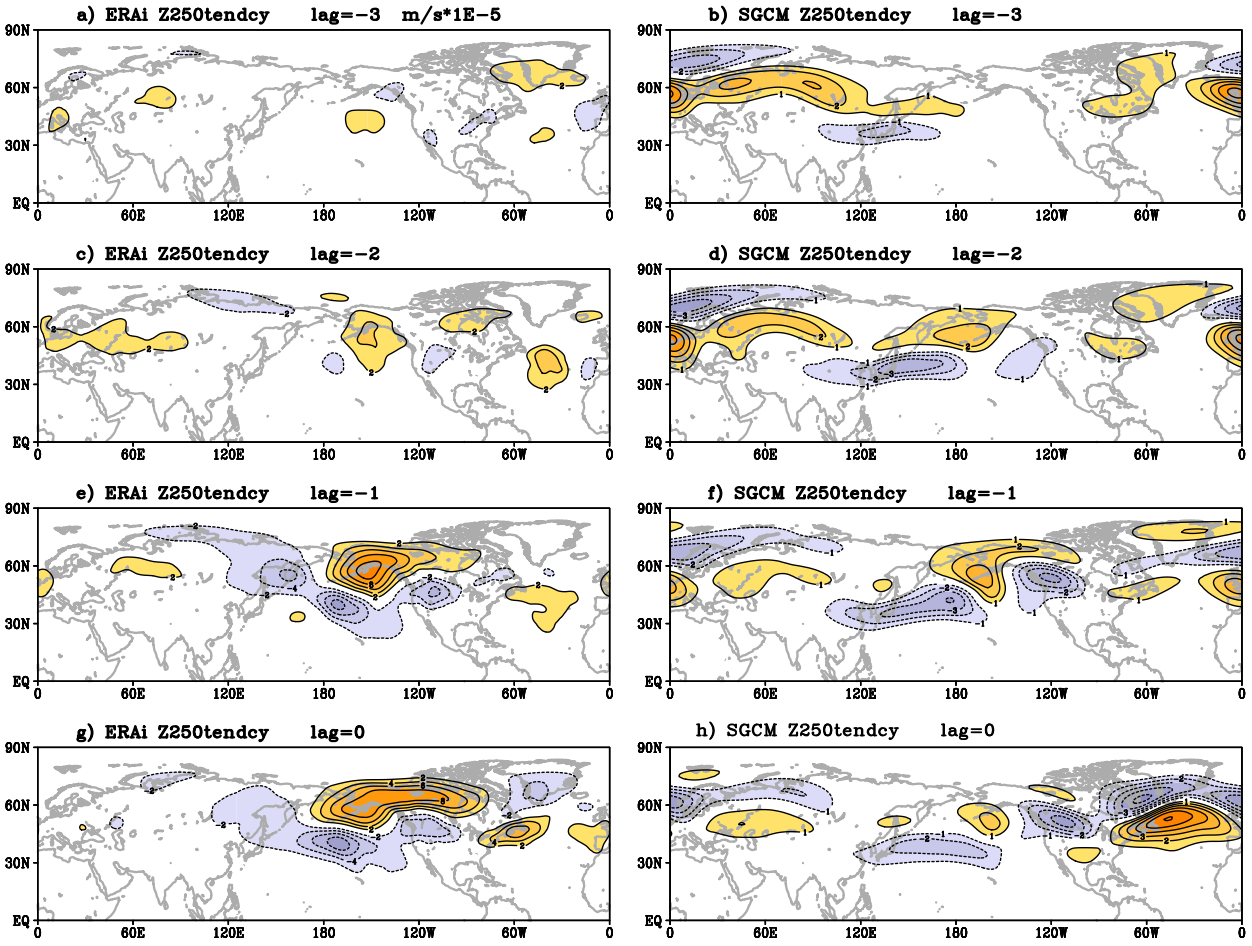

FIG. 9. Lead–lag regressions of the eddy induced geopotential height tendency at 250 hPa against PC1 for the (left) ERA-Interim and (right) SGCM simulation. The contour interval is 2×10^{-5} m s^{-1} for the left panels and 1×10^{-5} m s^{-1} for the right panels.

high-frequency synoptic-scale transient eddies. The barotropic feedback of these transients contributes constructively to the WACNA anomaly through vorticity flux convergence.

The analysis of the SGCM simulation suggests that the WACNA pattern is an intrinsic mode of surface air temperature variability. This, however, does not eliminate the role of climate change and slow variability in sea ice in influencing the characteristics of the WACNA mode. In reality, temperature variability of the polar center of WACNA will influence the surface heat flux which will lead to changes in sea ice. This results in a correlation between Arctic sea ice reduction and cold midlatitude temperature, as noted in previous studies (e.g., Guan et al. 2020b). It is possible that the changed sea ice cover will feedback to WACNA and further modify the intensity and duration of WACNA. The observed WACC in long-term trend and variability on decadal and interannual time scales may result from such feedback processes. Further studies would be needed to quantify the relative importance of this sea ice feedback. The snow-cover anomaly in Siberia may also contribute to WACNA as suggested in previous studies (e.g., Yu and Lin 2022). However, snow-cover variability may itself be a consequence of the internal WACC variability. As observed in Fig. 4, a positive WACNA is preceded by a negative WACE pattern with a warm anomaly in the south Siberian region which is associated with reduction of snow cover. Again, the changed snow cover will also feedback onto the circulation and influence WACNA, as demonstrated in Yu and Lin (2022).

Previous studies have also reported a possible connection between WACNA and the MJO (e.g., Lin 2015; Guan et al. 2020b). In the observations, about three pentads preceding a negative WACNA, the distribution of tropical outgoing longwave radiation (OLR) anomalies resembles the MJO phase 3, with enhanced convection in the Indian Ocean and suppressed convection in the tropical western Pacific (see Fig. 8 of Lin 2015). It is possible that Rossby waves induced by this tropical heating can propagate along the waveguide across the eastern North Pacific and influence the WACNA pattern. Further studies would be required to clarify this process and to assess its relative importance. Alternatively, it could be that tropical OLR anomalies about three pentads prior to WACNA are the result of some atmospheric process associated with the negative phase of WACE (Figs. 4a,b).

This study addresses WACNA variability on the intraseasonal time scale. We have shown that it can be characterized as

internal variability. However, this does not preclude a possible role for boundary forcing, which may amplify this low-frequency mode. Furthermore, the associated dynamical processes and mechanisms discussed here (Rossby wave propagation and transient feedback) are also relevant on longer time scales. The same WACNA pattern has been observed for the interannual and decadal time scales, and it is likely that for these longer time scales the feedback from the boundary forcing will be still more important for WACNA.

The WACNA mode does not seem sensitive to the details of the winter month average. We repeated the EOF analysis using the ERA-Interim data of DJF (rather than NDJFM as described above) and for an independent long SGCM integration with DJF forcing. Very similar EOF patterns as in Fig. 2 were obtained (not shown). It would be interesting to compare the intraseasonal features of the WACC mode under different basic states, e.g., El Niño versus La Niña, or for different periods of historical or projected global warming.

The existence of a WACNA pattern in the internal dynamics implies that the predictability and forecast skill of WACNA may be limited, as demonstrated in Lin (2018). On the other hand, since the kinetic energy conversion and wave propagation are linked to the slowly varying basic state, the predictability of the WACNA pattern may be flow dependent. It would be interesting to evaluate such flow-dependent predictability and forecast skill in operational dynamical models.

Acknowledgments. We thank Prof. Jacques Derome of McGill University for his internal review, which helped improve this manuscript.

Data availability statement. European Centre for Medium-Range Weather Forecasts (ECMWF) ERA-Interim dataset is available from https://www.ecmwf.int/en/forecasts/datasets/archive-datasets/reanalysis-datasets/era-interim.

REFERENCES

Blackport, R., J. A. Screen, K. van der Wiel, and R. Bintanja, 2019: Minimal influence of reduced Arctic sea ice on coincident cold winters in mid-latitudes. *Nat. Climate Change*, **9**, 697–704, https://doi.org/10.1038/s41558-019-0551-4.

Bretherton, C. S., M. Widmann, V. P. Dymnikov, J. M. Wallace, and I. Bladé, 1999: The effective number of spatial degrees of freedom of a time-varying field. *J. Climate*, **12**, 1990–2009, https://doi.org/10.1175/1520-0442(1999)012<1990:TENOSD>2.0.CO;2.

Clark, J. P., and S. Lee, 2019: The role of the tropically excited Arctic warming mechanism on the warm Arctic cold continent surface air temperature trend pattern. *Geophys. Res. Lett.*, **46**, 8490–8499, https://doi.org/10.1029/2019GL082714.

Cohen, J., M. Barlow, P. J. Kushner, and K. Saito, 2007: Stratosphere–troposphere coupling and links with Eurasian land surface variability. *J. Climate*, **20**, 5335–5343, https://doi.org/10.1175/2007JCLI1725.1.

——, and Coauthors, 2014: Recent Arctic amplification and extreme mid-latitude weather. *Nat. Geosci.*, **7**, 627–637, https://doi.org/10.1038/ngeo2234.

——, L. Agel, M. Barlow, C. I. Garfinkel, and I. White, 2021: Linking Arctic variability and change with extreme winter weather in the United States. *Science*, **373**, 1116–1121, https://doi.org/10.1126/science.abi9167.

Dee, D. P., and Coauthors, 2011: The ERA-Interim reanalysis: Configuration and performance of the data assimilation system. *Quart. J. Roy. Meteor. Soc.*, **137**, 553–597, https://doi.org/10.1002/qj.828.

Deser, C., R. A. Tomas, and S. Peng, 2007: The transient atmospheric circulation response to North Atlantic SST and sea ice anomalies. *J. Climate*, **20**, 4751–4767, https://doi.org/10.1175/JCLI4278.1.

Domeisen, D. I. V., and A. H. Butler, 2020: Stratospheric drivers of extreme events at the Earth's surface. *Commun. Earth Environ.*, **1**, 59, https://doi.org/10.1038/s43247-020-00060-z.

Francis, J. A., and S. J. Vavrus, 2012: Evidence linking Arctic amplification to extreme weather in mid-latitudes. *Geophys. Res. Lett.*, **39**, L06801, https://doi.org/10.1029/2012GL051000.

Guan, W., X. Jiang, X. Ren, G. Chen, and Q. Ding, 2020a: Role of atmospheric variability in driving the "warm-Arctic, cold-continent" pattern over the North America sector and sea ice variability over the Chukchi-Bering Sea. *Geophys. Res. Lett.*, **47**, e2020GL088599, https://doi.org/10.1029/2020GL088599.

——, ——, ——, ——, P. Lin, and H. Lin, 2020b: The leading intraseasonal variability mode of wintertime surface air temperature over the North American sector. *J. Climate*, **33**, 9287–9306, https://doi.org/10.1175/JCLI-D-20-0096.1.

Hall, N. M. J., 2000: A simple GCM based on dry dynamics and constant forcing. *J. Atmos. Sci.*, **57**, 1557–1572, https://doi.org/10.1175/1520-0469(2000)057<1557:ASGBOD>2.0.CO;2.

——, J. Derome, and H. Lin, 2001: The extratropical signal generated by a midlatitude SST anomaly. Part I: Sensitivity at equilibrium. *J. Climate*, **14**, 2035–2053, https://doi.org/10.1175/1520-0442(2001)014<2035:TESGBA>2.0.CO;2.

Henderson, S. A., E. D. Maloney, and S.-W. Son, 2017: Madden–Julian oscillation Pacific teleconnections: The impact of the basic state and MJO representation in general circulation models. *J. Climate*, **30**, 4567–4587, https://doi.org/10.1175/JCLI-D-16-0789.1.

Honda, M., J. Inoue, and S. Yamane, 2009: Influence of low Arctic sea-ice minima on anomalously cold Eurasian winters. *Geophys. Res. Lett.*, **36**, L08707, https://doi.org/10.1029/2008GL037079.

Hoskins, B. J., and A. J. Simmons, 1975: A multi-layer spectral model and the semi-implicit method. *Quart. J. Roy. Meteor. Soc.*, **101**, 637–655, https://doi.org/10.1002/qj.49710142918.

——, and T. Ambrizzi, 1993: Rossby wave propagation on a realistic longitudinally varying flow. *J. Atmos. Sci.*, **50**, 1661–1671, https://doi.org/10.1175/1520-0469(1993)050<1661:RWPOAR>2.0.CO;2.

——, I. N. James, and G. H. White, 1983: The shape, propagation and mean-flow interaction of large-scale weather systems. *J. Atmos. Sci.*, **40**, 1595–1612, https://doi.org/10.1175/1520-0469(1983)040<1595:TSPAMF>2.0.CO;2.

Kalnay, E., and Coauthors, 1996: The NCEP/NCAR 40-Year Reanalysis Project. *Bull. Amer. Meteor. Soc.*, **77**, 437–471, https://doi.org/10.1175/1520-0477(1996)077<0437:TNYRP>2.0.CO;2.

Kug, J.-S., J.-H. Jeong, Y.-S. Jang, B.-M. Kim, C. K. Folland, S.-K. Min, and S.-W. Son, 2015: Two distinct influences of Arctic warming on cold winters over North America and East Asia. *Nat. Geosci.*, **8**, 759–762, https://doi.org/10.1038/ngeo2517.

Lau, N.-C., 1988: Variability of the observed midlatitude storm tracks in relation to low-frequency changes in the circulation pattern. *J. Atmos. Sci.*, **45**, 2718–2743, https://doi.org/10.1175/1520-0469(1988)045<2718:VOTOMS>2.0.CO;2.

Lee, S. H., J. C. Furtado, and A. J. Charlton-Perez, 2019: Wintertime North American weather regimes and Arctic stratospheric polar vortex. *Geophys. Res. Lett.*, **46**, 14 892–14 900, https://doi.org/10.1029/2019GL085592.

Lin, H., 2015: Subseasonal variability of North American wintertime surface air temperature. *Climate Dyn.*, **45**, 1137–1155, https://doi.org/10.1007/s00382-014-2363-6.

——, 2018: Predicting the dominant patterns of subseasonal variability of wintertime surface air temperature in extratropical Northern Hemisphere. *Geophys. Res. Lett.*, **45**, 4381–4389, https://doi.org/10.1029/2018GL077509.

——, G. Brunet, and J. Derome, 2007: Intraseasonal variability in a dry atmospheric model. *J. Atmos. Sci.*, **64**, 2422–2441, https://doi.org/10.1175/JAS3955.1.

——, ——, and R. Mo, 2010: Impact of the Madden–Julian oscillation on wintertime precipitation in Canada. *Mon. Wea. Rev.*, **138**, 3822–3839, https://doi.org/10.1175/2010MWR3363.1.

Mori, M., M. Watanabe, H. Shiogama, J. Inoue, and M. Kimoto, 2014: Robust Arctic sea-ice influence on the frequent Eurasian cold winters in past decades. *Nat. Geosci.*, **7**, 869–873, https://doi.org/10.1038/ngeo2277.

——, Y. Kosaka, M. Watanabe, H. Nakamura, and M. Kimoto, 2019: A reconciled estimate of the influence of Arctic sea-ice loss on recent Eurasian cooling. *Nat. Climate Change*, **9**, 123–129, https://doi.org/10.1038/s41558-018-0379-3.

Overland, J. E., and M. Wang, 2010: Large-scale atmospheric circulation changes are associated with the recent loss of Arctic sea ice. *Tellus*, **62A**, 1–9, https://doi.org/10.1111/j.1600-0870.2009.00421.x.

——, K. R. Wood, and M. Wang, 2011: Warm Arctic-cold continents: Climate impacts of the newly open Arctic sea. *Polar Res.*, **30**, 15787, https://doi.org/10.3402/polar.v30i0.15787.

Park, M., and S. Lee, 2021: The role of planetary-scale eddies on the recent isentropic slope trend during boreal winter. *J. Atmos. Sci.*, **78**, 2879–2894, https://doi.org/10.1175/JAS-D-20-0348.1.

Screen, J. A., and R. Blackport, 2019: Is sea-ice-driven Eurasian cooling too weak in models? *Nat. Climate Change*, **9**, 934–936, https://doi.org/10.1038/s41558-019-0635-1.

——, I. Simmonds, C. Deser, and R. Tomas, 2013: The atmospheric response to three decades of observed Arctic sea ice loss. *J. Climate*, **26**, 1230–1248, https://doi.org/10.1175/JCLI-D-12-00063.1.

Sigmond, M., and J. C. Fyfe, 2016: Tropical Pacific impacts on cooling North American winters. *Nat. Climate Change*, **6**, 970–974, https://doi.org/10.1038/nclimate3069.

Simmons, A. J., J. M. Wallace, and G. W. Branstator, 1983: Barotropic wave propagation and instability, and atmospheric teleconnection patterns. *J. Atmos. Sci.*, **40**, 1363–1392, https://doi.org/10.1175/1520-0469(1983)040<1363:BWPAIA>2.0.CO;2.

Sorokina, S. A., C. Li, J. J. Wettstein, and N. G. Kvamstø, 2016: Observed atmospheric coupling between Barents Sea ice and the warm-Arctic cold-Siberian anomaly pattern. *J. Climate*, **29**, 495–511, https://doi.org/10.1175/JCLI-D-15-0046.1.

Soulard, N., H. Lin, J. Derome, and B. Yu, 2021: Tropical forcing of the circumglobal teleconnection pattern in boreal winter. *Climate Dyn.*, **57**, 865–877, https://doi.org/10.1007/s00382-021-05744-6.

Straus, D. M., S. Corti, and F. Molteni, 2007: Circulation regimes: Chaotic variability versus SST-forced predictability. *J. Climate*, **20**, 2251–2272, https://doi.org/10.1175/JCLI4070.1.

Sun, L. T., J. Perlwitz, and M. Hoerling, 2016: What caused the recent "warm Arctic, cold continents" trend pattern in winter temperatures? *Geophys. Res. Lett.*, **43**, 5345–5352, https://doi.org/10.1002/2016GL069024.

Takaya, K., and H. Nakamura, 2001: A formulation of a phase-independent wave-activity flux for stationary and migratory quasigeostrophic eddies on a zonally varying basic flow. *J. Atmos. Sci.*, **58**, 608–627, https://doi.org/10.1175/1520-0469(2001)058<0608:AFOAPI>2.0.CO;2.

Vigaud, N., A. W. Robertson, and M. K. Tippett, 2018: Predictability of recurrent weather regimes over North America during winter from submonthly reforecasts. *Mon. Wea. Rev.*, **146**, 2559–2577, https://doi.org/10.1175/MWR-D-18-0058.1.

Wallace, J. M., and D. S. Gutzler, 1981: Teleconnections in the geopotential height field during the Northern Hemisphere winter. *Mon. Wea. Rev.*, **109**, 784–812, https://doi.org/10.1175/1520-0493(1981)109<0784:TITGHF>2.0.CO;2.

Wilks, D. S., 2016: "The stippling shows statistically significant grid points": How research results are routinely overstated and overinterpolated, and what to do about it. *Bull. Amer. Meteor. Soc.*, **97**, 2263–2273, https://doi.org/10.1175/BAMS-D-15-00267.1.

Yu, B., and H. Lin, 2018: Coherent changes of wintertime surface air temperatures over North Asia and North America. *Sci. Rep.*, **8**, 5384, https://doi.org/10.1038/s41598-018-23750-3.

——, and ——, 2019: Modification of the wintertime Pacific–North American pattern related North American climate anomalies by the Asian–Bering–North American teleconnection. *Climate Dyn.*, **53**, 313–328, https://doi.org/10.1007/s00382-018-4586-4.

——, and ——, 2022: Interannual variability of the warm Arctic–cold North American pattern. *J. Climate*, **35**, 4277–4290, https://doi.org/10.1175/JCLI-D-21-0831.1.

——, ——, Z. Wu, and W. Merryfield, 2018: The Asian–Bering–North American teleconnection: Seasonality, maintenance, and climate impact on North America. *Climate Dyn.*, **50**, 2023–2038, https://doi.org/10.1007/s00382-017-3734-6.